

5 | The masses of satellites in GAMA galaxy groups from 100 square degrees of KiDS weak lensing data

We use the first 100 deg² of overlap between the Kilo-Degree Survey (KiDS) and the Galaxy And Mass Assembly (GAMA) survey to determine the galaxy halo mass of $\sim 10,000$ spectroscopically-confirmed satellite galaxies in massive ($M > 10^{13} h^{-1} M_{\odot}$) galaxy groups. Separating the sample as a function of projected distance to the group centre, we jointly model the satellites and their host groups with Navarro-Frenk-White (NFW) density profiles, fully accounting for the data covariance. The probed satellite galaxies in these groups have total masses $\log M_{\text{sub}}/(h^{-1} M_{\odot}) \approx 11.7 - 12.2$ consistent across group-centric distance within the errorbars. Given their typical stellar masses, $\log M_{\star, \text{sat}}/(h^{-2} M_{\odot}) \sim 10.5$, such total masses imply stellar mass fractions of $M_{\star, \text{sat}}/M_{\text{sub}} \approx 0.04 h^{-1}$. The average subhalo hosting these satellite galaxies has a mass $M_{\text{sub}} \sim 0.015 M_{\text{host}}$ independent of host halo mass, in broad agreement with the expectations of structure formation in a Λ CDM universe.

Cristóbal Sifón, Marcello Cacciato, Henk Hoekstra, et al., 2015, MNRAS, 454, 3938

5.1 Introduction

Following a hierarchical build-up, galaxy groups grow by accretion of smaller groups and isolated galaxies. Tidal interactions tend to transfer mass from infalling galaxies to the (new) host group, with the former becoming group satellites. The favoured cosmological scenario posits that galaxies are embedded in larger dark matter haloes, with masses that largely exceed the stellar masses, a conclusion supported by a variety of observations (see, e.g., the reviews by [Trimble 1987](#); [Einasto 2013](#)). Accordingly, satellite galaxies are hosted by ‘subhaloes,’ whose masses and distribution contain information on the properties of dark matter itself (e.g., [Libeskind et al. 2013](#)).

Because dark matter is (at least to a good approximation) dissipationless and baryons are not, it is subject to stronger tidal disruption than the baryonic component: energy losses cause baryons to sink to the centre of the potential more efficiently than dark matter, and therefore baryons are more resistant to tidal disruption ([White & Rees 1978](#)). This latter fact produces a unique prediction of the dark matter hypothesis: a satellite galaxy will be preferentially stripped of its dark, rather than stellar, matter. Thus, tidal stripping can be observed by comparing the total and stellar masses of satellite galaxies, such that galaxies accreted earlier have smaller mass-to-light ratios than galaxies accreted recently or (central) galaxies that have not been subject to tidal stripping by a larger host (e.g., [Chang et al. 2013a](#)).

Numerical simulations predict that tidal stripping is stronger within more centrally concentrated host haloes, and is more severe for more massive satellites (e.g., [Tormen et al. 1998](#); [Taffoni et al. 2003](#); [Contini et al. 2012](#)). Different infall timescales and concentrations induced by baryons (compared to dark matter-only simulations) can alter both the radial distribution and density profiles of subhaloes, consequently affecting tidal stripping in a radially-dependent manner ([Romano-Díaz et al. 2010](#); [Schewtschenko & Macciò 2011](#)), although this baryon-induced radial dependence could plausibly be (partially) compensated by feedback from active galactic nuclei (AGN; [Romano-Díaz et al. 2010](#)).

Observationally, the primary difficulty lies in estimating the total masses of satellite galaxies. Weak gravitational lensing is currently the only option available to measure the total mass of statistical samples of galaxies. So-called (weak) galaxy-galaxy lensing provides a direct measure of the masses of lensing galaxies through the observation of their distortion of the images of background galaxies, without assumptions about the dynamical state of the system (e.g., [Brainerd et al. 1996](#); [Courteau et al. 2014](#)). Weak lensing is an intrinsically statistical observational measurement: outside the strong lensing regime (typically a few tenths of arcsecond) the distortion induced in each background galaxy is much smaller than the typi-

cal galaxy ellipticity. Such measurements require high-quality multi-colour images that allow both accurate shape measurements and photometric redshift determination of faint, distant background sources. Measuring the lensing signal around satellite galaxies (hereafter ‘satellite lensing’, see, e.g., [Yang et al. 2006](#)) is particularly challenging because of i) the small relative contribution of the satellite galaxy to the lensing signal produced by the host galaxy group; ii) source blending at small separations, which hampers our ability to measure shapes reliably (and which is enhanced in high-density regions); and iii) particular sensitivity to contamination by field galaxies. This latter point is critical: since the dark matter haloes around satellite galaxies are expected to be stripped, isolated galaxies will significantly contaminate the lensing signal since they are not stripped, thus complicating a meaningful interpretation of the signal. Therefore, satellite lensing requires a clean sample of satellite galaxies to allow a proper interpretation of the signal. Satellite galaxies can usually be identified easily in massive galaxy clusters with high purity by use of, for instance, the red sequence (e.g., [Rozo et al. 2015](#), see also Chapter 4), which in principle requires only two-band photometry. Indeed, most satellite lensing measurements so far have concentrated on massive galaxy clusters with deep Hubble Space Telescope (HST) observations in which bright cluster members can be easily identified ([Natarajan et al. 2002](#); [Limousin et al. 2007](#); [Natarajan et al. 2009](#)), sometimes with the aid of strong lensing measurements ([Natarajan et al. 2007](#)). Some of these studies have claimed detections of satellite truncation, but it seems likely that they are mostly attributable to the parameterization of subhalo density profiles rather than direct detections ([Pastor Mira et al. 2011](#)).

Because galaxy groups have fewer satellites than massive clusters, lensing measurements of galaxy group satellites require larger samples and have only been possible thanks to recent large optical surveys with high image quality. Furthermore, because the red sequence is generally not so well established in galaxy groups compared to galaxy clusters, accurate group membership determination requires high-completeness spectroscopic observations. Lacking such data, most measurements in galaxy groups to date have relied on more indirect means of estimating subhalo masses. [Gillis et al. \(2013\)](#) used an optimized density estimator on galaxies selected from Canada-France-Hawaii Telescope Lensing Survey (CFHTLenS, [Heymans et al. 2012](#); [Erben et al. 2013](#)) and showed that the lensing signal of galaxies in high-density environments is inconsistent with the predictions of a model that does not include halo stripping, providing indirect evidence for tidal stripping in galaxy groups. Such differentiation was only possible because their high-density environment galaxies were mostly satellites, due to their carefully calibrated density estimator. Recently, [Li et al. \(2014\)](#) presented the first direct detection of the lensing signal from satellite galaxies in galaxy groups. They took advantage of

the overlap between deep imaging from the CFHT-Stripe82 Survey (CS82, e.g., Comparat et al. 2013) and the Sloan Digital Sky Survey (SDSS, York et al. 2000) Data Release 7 (Abazajian et al. 2009) spectroscopic catalogue. Yang et al. (2007) used this SDSS catalogue to construct a clean galaxy group catalogue with centrals and satellites identified individually; although Li et al. (2014) had only $\sim 1,000$ lens galaxies, their sample was essentially free of contamination by central galaxies. This allowed them to use weak lensing to directly measure the masses of satellites in galaxy groups for the first time, albeit with limited constraining power.

In this paper we present a direct measurement of the lensing signal from satellite galaxies in galaxy groups by combining a sample of spectroscopically confirmed galaxy groups from the Galaxy And Mass Assembly survey (GAMA, Driver et al. 2011), and background galaxies with high-quality shape measurements from the Kilo-Degree Survey (KiDS, de Jong et al. 2013; Kuijken et al. 2015). We use these measurements to constrain the masses of satellite galaxies as a function of projected distance from the group centre. By converting, in an average sense, these projected distances into 3-dimensional distances, we can study the evolution of satellite masses as they fall into galaxy groups.

This chapter is organized as follows. In Section 5.2 we describe the galaxy samples we use as lenses and lensed background sources. In Section 5.3 we summarize the measurement of galaxy-galaxy lensing and describe our modelling of satellites and their host groups. We present our results in Section 5.4 and summarize in Section 5.5. We adopt a flat Λ CDM cosmology with $\Omega_m = 0.315$, consistent with the latest cosmic microwave background measurements (Planck Collaboration 2015), and $H_0 = 100h \text{ km s}^{-1} \text{ Mpc}^{-1}$. We explicitly include the dependence on h where appropriate. Throughout we use the symbol $\langle X \rangle$ to refer to the median of distribution X .

5.2 Galaxy samples

5.2.1 Lens galaxies: satellites in the GAMA galaxy group catalogue

GAMA¹ is a spectroscopic survey which measured redshifts for 238,000 galaxies over a total of 286 deg^2 carried out with the AAOmega spectrograph on the Anglo-Australian Telescope (AAT). GAMA is 98% spectroscopically complete down to $m_r = 19.8$ even in the most crowded regions (Baldry et al. 2010; Driver et al. 2011; Liske et al. 2015). Here we use data over three different regions on the sky, centred at right ascensions 9h, 12h and 15h (the G09, G12 and G15 fields), which overlap with SDSS data. Below we briefly describe the GAMA galaxy group

¹<http://www.gama-survey.org/>

sample constructed by [Robotham et al. \(2011\)](#), who discuss the properties, possible systematics, and limitations of the catalogue in greater detail. Galaxy photometric properties such as luminosity and stellar mass are measured from the five-band optical SDSS imaging. In particular, we use the stellar masses derived by [Taylor et al. \(2011\)](#) by fitting [Bruzual & Charlot \(2003\)](#) synthetic stellar spectra to the broadband SDSS photometry.

The GAMA galaxy group catalogue was constructed using a 3-dimensional Friends-of-Friends (FoF) algorithm, linking galaxies in projected and line-of-sight separations. We use version 7 of the group catalogue (G³Cv7), which contains 23,838 groups with $N_{\text{FoF}} \geq 2$, where N_{FoF} is the number of spectroscopic members grouped together by the FoF algorithm (each group has $N_{\text{FoF}} - 1$ satellites). Group properties such as velocity dispersion and total luminosity² were calibrated to mock galaxy catalogues processed in the same way as the real data and were optimized for groups with $N_{\text{FoF}} \geq 5$. A visual inspection of the phase space (distance-velocity plane) of GAMA groups confirms that groups with $N_{\text{FoF}} < 5$ are significantly contaminated by interlopers, while member selection for groups with $N_{\text{FoF}} \geq 5$ is in better agreement with the expectation of a smooth distribution of galaxies with a maximum velocity that decreases with radius (e.g., [Mamon et al. 2010](#)). We therefore restrict our study to groups with $N_{\text{FoF}} \geq 5$, in the 68.5 deg² of unmasked area overlapping with the first release of KiDS lensing data (see [Section 5.2.2](#)). In all, we use 9683 satellites hosted by 1467 different groups³. These are the same groups used by [Viola et al. \(2015\)](#).

[Robotham et al. \(2011\)](#) identified the central galaxy in each group using three definitions of group centre: the weighted centre of light, an iterative method rejecting the galaxy farthest away from the center of light until one galaxy remained (the ‘iterative’ centre), and the brightest cluster galaxy (hereafter BCG). All galaxies that are not centrals are classified as satellites. In most cases ($\sim 90\%$) the iterative central galaxy coincides with the BCG, while the centre of light is more discrepant. [Viola et al. \(2015\)](#) performed a detailed analysis of the lensing signal of GAMA groups comparing the different centre definitions and confirm the results of [Robotham et al. \(2011\)](#): the BCG and the iterative centre both represent the group centre of mass to a good degree, while the centre of light is a very poor indicator of the group centre. In this work we use the central-satellite classification that uses the BCG as the central, and therefore measure the lensing signal around all group members

²The total luminosity of a group is the sum of the luminosities of its member galaxies, corrected for spectroscopic incompleteness at the low-mass end (see [Robotham et al. 2011](#)).

³This is the total number of satellites considered in this work, and includes satellites that do not fall within the currently available KiDS data but reside in a group which is less than $2 h^{-1} \text{Mpc}$ away from the center of the closest KiDS field. 9357 (97%) of these satellites fall within the KiDS footprint (see [Table 5.1](#)).

Table 5.1: Median properties of satellite galaxies binned by projected distance to the group centre, R_{sat} . N_{sat} is the total number of satellites considered while $N_{\text{sat}}^{\text{KiDS}}$ is the number of satellites that fall within the 100 deg^2 of KiDS imaging used in this work. Errorbars are 16th and 84th percentiles.

Bin	R_{sat} range ($h^{-1}\text{Mpc}$)	N_{host}	N_{sat}	$N_{\text{sat}}^{\text{KiDS}}$	$\langle N_{\text{FoF}} \rangle$	$\langle R_{\text{sat}} \rangle$ ($h^{-1}\text{Mpc}$)	$\langle z_{\text{sat}} \rangle$	$\log \langle M_{\star, \text{sat}} \rangle$ ($h^{-2}M_{\odot}$)	$\log \langle L_{\text{host}} \rangle$ ($h^{-2}L_{\odot}$)
1	0.05 – 0.20	1263	3714	3541	7^{+5}_{-2}	$0.12^{+0.05}_{-0.05}$	$0.17^{+0.09}_{-0.09}$	$10.45^{+0.26}_{-0.09}$	$11.10^{+0.17}_{-0.23}$
2	0.20 – 0.35	1235	3152	3042	7^{+5}_{-2}	$0.25^{+0.05}_{-0.04}$	$0.19^{+0.10}_{-0.09}$	$10.51^{+0.22}_{-0.10}$	$11.15^{+0.14}_{-0.26}$
3	0.35 – 1.00	785	2817	2773	8^{+7}_{-3}	$0.43^{+0.16}_{-0.08}$	$0.21^{+0.10}_{-0.07}$	$10.66^{+0.15}_{-0.14}$	$11.33^{+0.10}_{-0.25}$

except the BCGs.

5.2.2 Lensed background sources: the Kilo-Degree Survey

KiDS⁴ is an ESO Public Survey being conducted with the 2.6 m VLT Survey Telescope (VST) in Cerro Paranal, Chile, which surveys the sky in the *ugri* bands. Each 1 deg² pointing is observed four times (‘exposures’) in the *u*-band and five times in the other bands. Upon completion, KiDS will cover 1,500 deg²: half of the survey area will be on a 9°-wide patch around the celestial equator and the other half on a similarly-shaped region around a declination of -31° (de Jong et al. 2013). In total, KiDS overlaps with four GAMA patches: three in the equator (the three used in this work) and one in the south (G23), for a total of 240 deg². In this work, we use an unmasked area of 68.5 deg² over ~ 100 deg² of overlap currently available (de Jong et al. 2015).

KiDS data were reduced using two different pipelines: a reduction based on Astro-WISE (McFarland et al. 2013) used to measure Gaussian-weighted aperture photometry (Kuijken 2008) and photometric redshifts with the Bayesian Photometric Redshift (BPZ) code (Benítez 2000), and a theli reduction (Erben et al. 2013) used to measure galaxy shapes with *lensfit* (Miller et al. 2007, 2013; Kitching et al. 2008). We briefly describe each in the following and refer to de Jong et al. (2015) and Kuijken et al. (2015) for details, including tests of systematic effects on shape measurements and photometric redshifts.

5.2.2.1 Photometric redshifts

Photometric redshifts use the coadded images from the KiDS public data releases DR1 and DR2 (de Jong et al. 2015) as input. These were processed using a pipeline largely based on the Astro-WISE optical pipeline (McFarland et al. 2013) which includes crosstalk and overscan corrections, flat fielding, illumination correction, satellite track removal and background subtraction, plus masking for bad pixels, saturation spikes and stellar haloes. A common astrometric solution was calculated per filter using a second-order polynomial. Individual exposures were regridded and co-added using a weighted mean procedure. Photometric zero-points were first derived per CCD by comparing nightly standard star observations to SDSS DR8 (Aihara et al. 2011) and zero-point offsets were subsequently applied to the *gri* data, based on a comparison of the photometry between the CCDs in the five exposures. This yields a homogeneous photometry over 1 deg².

The point spread function (PSF) of the stacked images was homogenized by convolving them with a Gaussian kernel with varying width, such that each re-

⁴<http://kids.strw.leidenuniv.nl/>

sulting image has a circular, Gaussian PSF with constant width across the field of view. A ‘Gaussian Aperture and PSF’ (GAaP, Kuijken 2008) photometry can be obtained such that the resulting aperture photometry is independent of seeing (see Appendix A of Kuijken et al. 2015). The flux of a galaxy can then be measured consistently within the same physical aperture in all bands, which is necessary for unbiased galaxy colour estimates.

GAaP photometry was finally compared to SDSS photometry in order to obtain an absolute photometric calibration. Photometric redshifts were estimated using GAaP magnitudes with BPZ, following Hildebrandt et al. (2012). Kuijken et al. (2015) compared the photometric redshifts to $\sim 17,000$ spectroscopic redshifts in the zCOSMOS (Lilly et al. 2007) and ESO/GOODS (Vanzella et al. 2008; Balestra et al. 2010) surveys. They found that the peak of the posterior distribution, z_B , is biased by less than 2% in the range $0.005 < z_B < 1.0$. However, for lenses at $z_l \lesssim 0.3$, as in our case, the lensing efficiency (cf. Equation 5.2) does not vary significantly for sources beyond $z_s = 0.5$. In order to have a larger number of sources for which to measure shapes, we therefore use all galaxies in the range $0.005 < z_B < 1.2$. In the context of the CFHTLenS survey, Benjamin et al. (2013) have shown that the stacked photometric redshift posterior distribution, $p(z)$, estimated by Hildebrandt et al. (2012) in this z_B range is a fair representation of the true (i.e., spectroscopic) redshift distribution. We therefore use the full $p(z)$ in our lensing analysis (see Section 5.3).

5.2.2.2 Shape measurements

The r -band data were also reduced with the theli pipeline (Erben et al. 2013), independently of the Astro-WISE pipeline, in order to measure the shapes of galaxies. We used only the r -band data for shape measurements, since the r -band observing conditions are significantly better than in the other three bands (see de Jong et al. 2013); combining different bands is not expected to result in a useful improvement in shape measurements. We used SExtractor (Bertin & Arnouts 1996) to detect objects on the stacked r -band image, and used the resulting catalogue as input to *lensfit*, which is used to simultaneously analyze the single exposures. *Lensfit* is a Bayesian method that returns for each object an ellipticity and an associated weight, w_s , which quantifies the measurement uncertainty after marginalizing over galaxy position, size, brightness, and bulge-to-disk ratio. It interpolates the PSF over a 2-dimensional polynomial across the image in order to estimate the PSF at the location of each galaxy. The number density of galaxies in the unmasked region that pass the photometric redshift cuts having $w_s > 0$ is $n_{\text{gal}} = 8.88 \text{ gal arcmin}^{-2}$ and the effective number of galaxies is $n_{\text{eff}} = (\sigma_\epsilon/A) \sum_i w_{s,i} = 4.48 \text{ gal arcmin}^{-2}$ (see Chang et al. 2013b; Kuijken

et al. 2015); the root-mean-square (rms) ellipticity of galaxies is $\sigma_\epsilon = 0.279$. We correct for *noise bias*, which produces a signal-to-noise ratio (S/N) -dependent correction factor, m , between the mean ellipticity measurements and the shear (e.g., Melchior & Viola 2012; Refregier et al. 2012; Viola et al. 2014, see Section 5.3), using the correction calculated for CFHTLenS using extensive image simulations by Miller et al. (2013), which Kuijken et al. (2015) demonstrate is appropriate for the current KiDS catalogue. We also correct the galaxy shapes for an additive bias, c , introduced by imperfect PSF modelling following Heymans et al. (2012). See Kuijken et al. (2015) for details.

In performing the lensing analysis we have decided to blind ourselves to the final results. By doing this we ensure that the analysis does not depend on the results, and minimize the risk of confirmation bias. This is an especially important concern in this era of precision cosmology. At the start of the project we contacted an external person (unknown to all members of the KiDS collaboration except for the contact person), who generated three additional catalogues by rescaling the galaxy ellipticities by factors unknown to us. We carried out the full analysis four times, one for each ellipticity catalogue. Only when the team was convinced about the analysis *carried out with the four ellipticity catalogues*, the analysis was frozen *with no further changes to the results* and we contacted the external person again to reveal the true catalogue. A detailed description of the shape analysis and catalogue blinding of KiDS data is given in Kuijken et al. (2015).

5.3 Galaxy-galaxy lensing of satellite galaxies

Gravitational lensing produces a differential deflection of light coming from background galaxies when it passes through an inhomogeneous mass distribution, and most strongly along a mass concentration. The observable effect is a coherent distortion on both the shape and the size of background sources around the lens. The shape distortion, γ_t , is referred to as *shear*, and in the weak lensing limit is much smaller than the typical ellipticities of galaxies and can only be measured statistically by averaging over many background sources. The average tangential shear relates to the excess surface mass density (ESD) at a projected distance⁵ R of the lens, $\Delta\Sigma(R)$, through

$$\Delta\Sigma(R) \equiv \bar{\Sigma}(< R) - \bar{\Sigma}(R) = \Sigma_c \gamma_t(R), \quad (5.1)$$

where $\bar{\Sigma}(< R)$ is the average surface density within R , $\bar{\Sigma}(R)$ is the average surface density *at* R (more precisely, within a thin shell $R + \delta R$) and the critical density,

⁵As a convention, we list 3-dimensional distances in groups with lower case r , and distances projected in the plane of the sky with capital R .

Σ_c , is as a geometrical factor that accounts for the lensing efficiency,

$$\Sigma_c = \frac{c^2}{4\pi G} \frac{D(z_s)}{D(z_l)D(z_l, z_s)}. \quad (5.2)$$

Here, $D(z_l)$, $D(z_s)$, and $D(z_l, z_s)$ are the angular diameter distances to the lens, to the source and between the lens and the source, respectively. Therefore the redshifts of the lenses and sources are essential to relate the tangential distortions of the sources to the projected mass density of the lens.

We calculate $D(z_l)$ for each lens galaxy using its spectroscopic redshift from GAMA and marginalize over the full probability distribution of the photometric redshift of each background source, $p(z_s)$. Specifically, for every lens-source pair we calculate

$$\tilde{\Sigma}_{c,ls}^{-1} = \frac{4\pi G}{c^2} D(z_l) \int_{z_l}^{\infty} dz_s p(z_s) \frac{D(z_l, z_s)}{D(z_s)}. \quad (5.3)$$

Each lens-source pair is then assigned a weight that combines the *lensfit* weight and the lensing efficiency,

$$w_{ls} = w_s \tilde{\Sigma}_{c,ls}^{-2}. \quad (5.4)$$

The ESD in a bin centred on a projected distance R is then calculated as

$$\Delta\Sigma(R) = \left(\frac{\sum_{ls} w_{ls} \epsilon_t \tilde{\Sigma}_{c,ls}}{\sum_{ls} w_{ls}} \right) \frac{1}{1 + K(R)} \quad (5.5)$$

where the sum is over all lens-source pairs in the radial bin, ϵ_t is the tangential component of the ellipticity of each source around each lens, and

$$K(R) = \frac{\sum_{ls} w_{ls} m_s}{\sum_{ls} w_{ls}} \simeq 0.1, \quad (5.6)$$

where m is the multiplicative correction for noise bias (Miller et al. 2013; Kuijken et al. 2015).

The ESD around a satellite galaxy at a projected distance R_{sat} from the group centre, $\Delta\Sigma_{\text{sat}}(R|R_{\text{sat}})$, is given by

$$\Delta\Sigma_{\text{sat}}(R|R_{\text{sat}}) = \Delta\Sigma_{\text{sub}}(R) + \Delta\Sigma_{\text{host}}(R|R_{\text{sat}}), \quad (5.7)$$

where $\Delta\Sigma_{\text{sub}}$ is the ESD of the subhalo in which the satellite galaxy resides and $\Delta\Sigma_{\text{host}}$ is the ESD of the host galaxy group, measured around the satellite galaxy. We describe the measured satellite lensing signal in Section 5.3.1 before discussing our modelling of both terms of Equation 5.7 in Sections 5.3.2 and 5.3.3. In doing this, we follow the discussion by Yang et al. (2006).

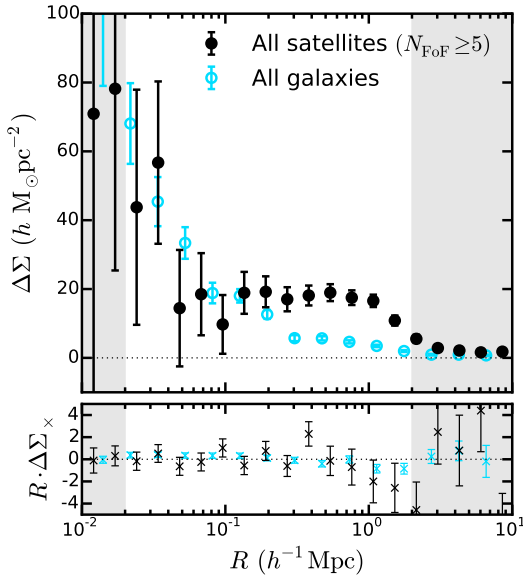


Figure 5.1: Top: Excess surface density around all satellites residing in groups with $N_{\text{FoF}} \geq 5$ (black points) and around all galaxies in the GAMA catalogue (cyan circles). Bottom: corresponding cross signals, multiplied by projected separation, R , to make the errorbars of comparable size throughout the radial range (units are omitted for clarity). Dotted horizontal lines in both panels show $\Delta\Sigma = 0$. We used different bins to measure the signal of each sample for clarity. The grey bands show projected separations that are not used in our analysis.

5.3.1 The satellite lensing signal

We show in [Figure 5.1](#) the stacked ESD of all 9683 satellites residing in groups with $N_{\text{FoF}} \geq 5$. We also show the ESD around all galaxies in the GAMA catalogue, which is dominated by (central) field galaxies ([Robotham et al. 2011](#)). The lensing signal around the two samples is qualitatively different. In terms of [Equation 5.7](#), the ESD of central galaxies can be described by $\Delta\Sigma_{\text{host}}(R|R_{\text{sat}} = 0)$ alone (see [?](#) for a detailed comparison of the lensing signal of different lens samples). The bottom panel of [Figure 5.1](#) shows $\Delta\Sigma_{\times}$, which is defined analogously to [Equation 5.1](#) using the shear measured at 45° rotations from the direction tangential to the lens. $\Delta\Sigma_{\times}$ should be consistent with zero because of parity symmetry ([Schneider 2003](#)), and therefore serves as a check for systematic effects. As shown in [Figure 5.1](#), $\Delta\Sigma_{\times}$ is consistent with zero for both samples at all lens-source separations.

Although in [Figure 5.1](#) we show the lensing signal for separations $0.01 \leq R/(h^{-1}\text{Mpc}) \leq 10$, we only use measurements of $\Delta\Sigma$ in the range $0.02 \leq R/(h^{-1}\text{Mpc}) \leq 2$ in our analysis. Separations outside this range are marked in [Figure 5.1](#) by grey bands. At smaller separations, blending with and obscuration by group members become significant and therefore the S/N is very low; at larger separations the coverage is highly incomplete due to the patchiness of the current KiDS data, making measurements less reliable. We assess the effect of the patchy coverage by measuring the lensing signal around random locations on the images, which should be consistent with zero. The signal is indeed consistent with

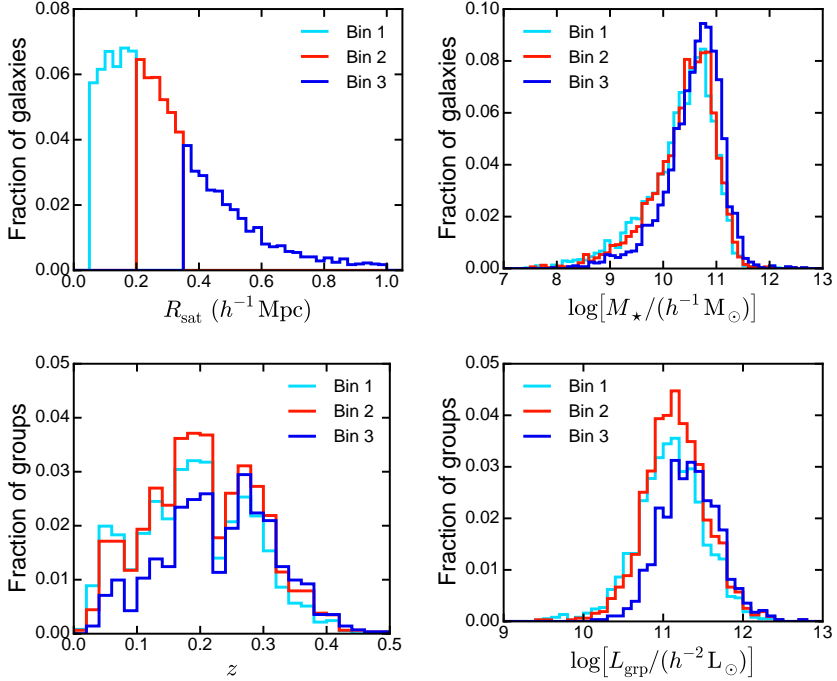


Figure 5.2: Top: Satellite distributions of distance to the BCG (left) and stellar mass (right); bottom: Group distributions of redshift (left) and total luminosity (right); for the radial bins defined in Table 5.1. Note that each group can contribute to more than one bin in the lower panels.

zero for separations $R \lesssim 5 h^{-1} \text{Mpc}$, but at separations $R \gtrsim 5 h^{-1} \text{Mpc}$ the lensing signal around random points deviates significantly from zero (see Viola et al. 2015). This indicates that systematic effects are affecting the shear estimation at such distances. We do not try to correct for such effects and instead conservatively discard measurements at separations $R > 2 h^{-1} \text{Mpc}$.

The errorbars in Figure 5.1 correspond to the square root of the diagonal elements of the covariance matrix, described in Section 5.A. In principle, the lensing covariance matrix includes contributions from shape noise and sample (‘cosmic’) variance. Shape noise arises because galaxies are intrinsically elliptic and because noise in the images introduces additional uncertainties in the shape measurements (see, e.g., Hoekstra et al. 2000), while sample variance accounts for the finite fraction of the sky observed. As we show in Section 5.A, the contribution from sample variance can be safely neglected for our purposes and we therefore include only the contribution from shape noise, which can be calculated directly from the data

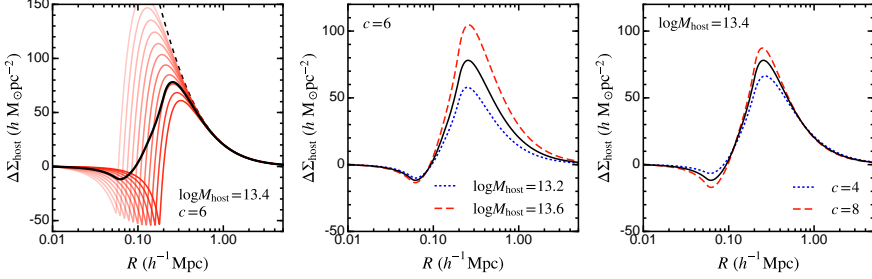


Figure 5.3: Illustration of the contribution from the host group, $\Delta\Sigma_{\text{host}}(R|n(R_{\text{sat}}))$, to Equation 5.7. Left: Red lines show the contribution to the signal around satellites at different distances from the group centre in logarithmic bins, with opacity scaling with the number densities of objects in each bin, $n(R_{\text{sat}})$, corresponding to the cyan histogram in the top-left panel of Figure 5.2. The thick black line is the weighted average of the red lines (cf. Equation 5.12) and represents the group contribution to the lensing signal around our sample of satellites with $0.05 \leq R_{\text{sat}}/(h^{-1}\text{Mpc}) \leq 0.20$ in a group with $\log M_{200} = 13.4$ and $c = 6$, and is reproduced in the middle and right panels. The black dashed line shows the excess surface density of the same group when measured around the group centre. Middle: Varying group mass at fixed concentration. Right: Varying group concentration at fixed mass. Note that the vertical scale in the middle and right panels is zoomed in with respect to the left panel. All masses are in units of $h^{-1}M_{\odot}$.

(see Section 3.4 of Viola et al. 2015). In addition to the covariance between data points (as in the case of Figure 5.1), we also compute the covariance between data points around lenses in different bins of projected distance from the group centre, R_{sat} (see Figure 5.8).

The signal shown in Figure 5.1 has a high S/N, but its interpretation is complicated by the mixing of satellites with a wide range of properties. van Uitert et al. (2016) use this satellite sample to study the stellar-to-halo mass relation by binning the sample in stellar mass and redshift. Here, we bin the sample by projected distance to the group centre; this binning is shown in the top-left panel of Figure 5.2 (see also Table 5.1). We find that this particular binning allows us to study each bin with high enough S/N. We take the distance from the group centre as a proxy for time since infall to the group (e.g., Gao et al. 2004; Chang et al. 2013a) and study the evolution of the mass in satellites as these galaxies interact with their host groups. As shown in Figure 5.2 (top right), the three radial bins have similar stellar mass distributions, their medians differing by only 0.2 dex (Table 5.1). In contrast, the group redshift and luminosity distributions of bin 3 are different from the other two bins. Because we separate groups by satellite distance, we essentially split groups by size. Only the most massive (i.e., the most luminous) groups in the sample have satellites at $R_{\text{sat}} > 0.35 h^{-1}\text{Mpc}$. Additionally, because GAMA is a

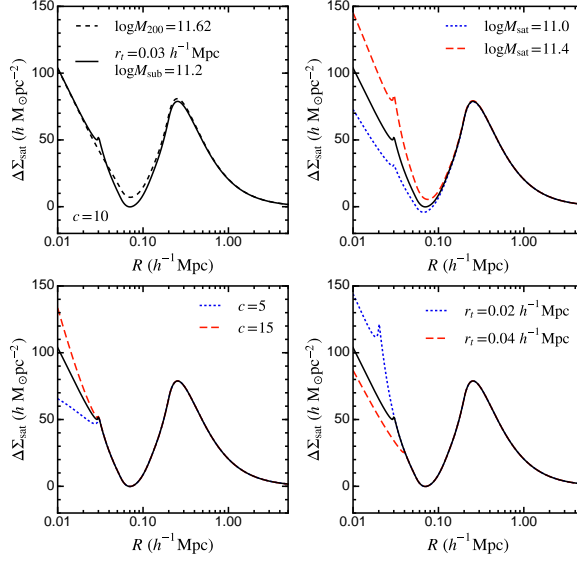


Figure 5.4: The satellite lensing signal, $\Delta\Sigma_{\text{sat}}$, for different satellite properties. The group contribution is kept fixed at the fiducial value (i.e., the thick solid line) from [Figure 5.3](#). Top left: The dashed line shows the excess surface density of a NFW profile with $c = 10$ and $\log M_{200} = 11.62$. Truncating this profile through [Equation 5.15](#) at $r_t = 0.03 h^{-1} \text{Mpc} \approx 2.6 r_s$ produces the solid line, with a total mass $\log M_{\text{sub}} = 11.2$, which is reproduced in all other panels. The glitch in the solid line is produced by the sharp truncation of the density profile and is continuous but non-differentiable. Top right: Varying M_{sub} , keeping both $c = 10$ and $r_t = 0.03 h^{-1} \text{Mpc}$ fixed. Bottom left: Varying the concentration, keeping both $\log M_{\text{sub}} = 11.2$ and $r_t = 0.03 h^{-1} \text{Mpc}$ fixed. Bottom right: Varying the truncation radius, keeping both $c = 10$ and $\log M_{\text{sub}} = 11.2$ fixed. Note that the normalization of the inner profile changes because we fix the mass *within the truncation radius*, which is itself changing. All masses are in units of $h^{-1} M_{\odot}$.

magnitude-limited survey, groups at high redshift are on average more luminous (i.e., more massive), which causes the different redshift distributions.

5.3.2 Host group contribution

The average density profile of galaxy groups is well described by a Navarro-Frenk-White (NFW, [Navarro et al. 1995](#)) profile,

$$\rho_{\text{NFW}}(r) = \frac{\delta_c \rho_m}{(r/r_s)(1 + r/r_s)^2}, \quad (5.8)$$

where $\rho_m(z) = 3H_0^2(1+z)^3\Omega_M/(8\pi G)$ is the mean density of the Universe at redshift z and

$$\delta_c = \frac{200}{3} \frac{c^3}{\ln(1+c) - c/(1+c)}. \quad (5.9)$$

The two free parameters, r_s and $c \equiv r_{200}/r_s$, are the scale radius and concentration of the profile, respectively. However, we use the concentration and the mass⁶, M_{200} , as the free parameters for convenience. We further assume the mass-concentration relation, $c(M, z)$, of [Duffy et al. \(2008\)](#), allowing for a free normalization, f_c^{host} . That is,

$$c(M_{200}, z) = f_c^{\text{host}} \left[10.14 \left(\frac{M_{200}}{2 \times 10^{12} h^{-1} M_\odot} \right)^{-0.089} (1+z)^{-1.01} \right]. \quad (5.10)$$

The average surface density of the host group measured at a projected distance R_{sat} from the group centre is simply the azimuthal average of Σ_{host} around the satellite,

$$\bar{\Sigma}_{\text{host}}(R|R_{\text{sat}}) = \frac{1}{2\pi} \int_0^{2\pi} d\theta \Sigma_{\text{NFW}} \left(\sqrt{R_{\text{sat}}^2 + R^2 + 2RR_{\text{sat}} \cos \theta} \right), \quad (5.11)$$

and the contribution to the satellite ESD follows from [Equation 5.1](#). We use the analytical expression for the projected surface density of an NFW profile, $\Sigma_{\text{NFW}}(R)$, derived by [Wright & Brainerd \(2000\)](#).

In reality we observe a sample of satellites at different distances to their respective group centres; therefore the total group contribution is

$$\Delta\Sigma_{\text{host}}(R|n(R_{\text{sat}})) = \frac{\int_{R_{\text{sat}}^{\text{min}}}^{R_{\text{sat}}^{\text{max}}} dR_{\text{sat}} n(R_{\text{sat}}) \Delta\Sigma_{\text{host}}(R|R_{\text{sat}})}{\int_{R_{\text{sat}}^{\text{min}}}^{R_{\text{sat}}^{\text{max}}} dR_{\text{sat}} n(R_{\text{sat}})}, \quad (5.12)$$

where $n(R_{\text{sat}})$ is the number density of satellites at R_{sat} . We use [Equation 5.12](#) to model the host group contribution to [Equation 5.7](#) throughout. Our implementation differs from that introduced by [Yang et al. \(2006\)](#) and applied by [Li et al. \(2014\)](#) in that they fit for R_{sat} , whereas we use the measured separations to fix $n(R_{\text{sat}})$.

We illustrate the difference between $\Delta\Sigma_{\text{host}}(R|R_{\text{sat}})$ and $\Delta\Sigma_{\text{host}}(R|n(R_{\text{sat}}))$ in the left panel of [Figure 5.3](#), for the innermost bin considered in this work (see [Table 5.1](#) and the top left panel of [Figure 5.2](#)). The left panel of [Figure 5.3](#) shows that $\Delta\Sigma_{\text{host}}(R|R_{\text{sat}})$ of a single group-satellite pair has a sharp minimum at $R = R_{\text{sat}}$ where $\Sigma(R)$ is maximal and therefore $\Delta\Sigma < 0$; $\Delta\Sigma_{\text{host}}(R|R_{\text{sat}})$ increases

⁶Here M_{200} is the mass within a radius r_{200} , which encloses a density $\rho(< r_{200}) = 200\rho_m(z)$.

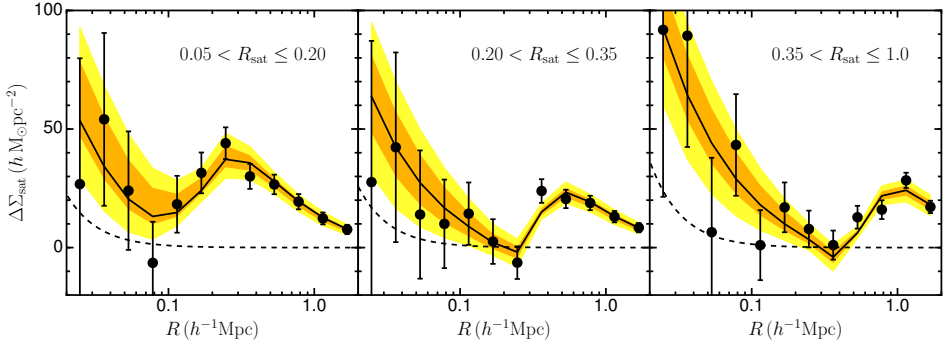


Figure 5.5: Excess surface density around satellite galaxies in the three radial bins summarized in Table 5.1 and shown in the legends in units of $h^{-1}\text{Mpc}$. Black points show lensing measurements around GAMA group satellites using KiDS data; errorbars correspond to the square root of the diagonal elements of the covariance matrix. The solid black line is the best-fit model where subhaloes are modelled as having NFW density profiles, and orange and yellow shaded regions mark 68% and 95% credible intervals, respectively. Dashed lines show the contribution of a point mass with a mass equal to the median stellar mass of each bin, which is included in the model.

abruptly further out and then drops back to the group’s outer profile, matching the group profile measured around the group centre. Accounting for the distribution of group-centric distances shifts this minimum to $R < \langle R_{\text{sat}} \rangle$, and makes both the peak and the dip significantly less pronounced; including the distribution of projected distances is critical to properly model the statistical properties of the lensing signal which cannot be captured by fitting for an average value. Similarly, the middle and right panels of Figure 5.3 show the effect of different host masses and concentrations on $\Delta\Sigma_{\text{host}}(R|n(R_{\text{sat}}))$. A higher mass increases its amplitude at all scales where the host contribution dominates, whereas a higher concentration mostly enhances the ESD signal around the peak and produces a more pronounced dip.

Our model ignores the contribution from baryons in the central group galaxy, which are noticeable at scales $R < 0.05 h^{-1}\text{Mpc}$ (Viola et al. 2015). Because baryons are more concentrated than dark matter, they can make the total density profile steeper than a pure NFW. Viola et al. (2015) have shown, however, that the amplitude of the baryonic contribution (modelled as a point mass) is not degenerate with any other group parameter in their halo model. Therefore we expect baryons in the BCG to have no impact on our results.

5.3.3 Satellite contribution

Pastor Mira et al. (2011) studied the density profiles of subhaloes in the Millenium simulation (Springel et al. 2005) and found that they are well fit by an NFW profile, with no evidence for truncation at any separation from the group centre. As discussed by Hayashi et al. (2003), while tidal disruption removes mass preferentially from the outskirts, tidal heating causes the subhalo to expand after every orbit. The two effects compensate in terms of the density distribution such that a defined truncation radius cannot be discerned in subhaloes. We therefore model subhaloes as NFW profiles (Equation 5.8). We assume the $c(M, z)$ relation of Duffy et al. (2008); in analogy to Equation 5.10, we set $f_c^{\text{sub}} = 1$. To account for the baryonic contribution to the subhalo mass, we include a point mass in the centre with a mass equal to the median stellar mass for each bin (Table 5.1). Our model for the satellites therefore has a single free parameter per radial bin, namely $M_{\text{sub}}(< r_{200})$.

For comparison, we also implement a theoretically-motivated model where subhaloes are tidally stripped by the host potential. In this model, a subhalo in a circular orbit is truncated at the radius at which the accelerations due to the tidal force from the host halo equals that arising from the gravitational force of the subhalo itself. This radius is given by

$$r_t = \left[\frac{M_{\text{sub}}(< r_t)}{(3 - \partial \ln M / \partial \ln r) M_{\text{host}}(< r_{\text{sat}})} \right]^{1/3} r_{\text{sat}} \quad (5.13)$$

(King 1962; Binney & Tremaine 1987; Mo et al. 2010), where, for an NFW profile,

$$\frac{\partial \ln M_{\text{NFW}}}{\partial \ln r} = \frac{r^2}{(r_s + r)^2} \left[\ln \left(\frac{r_s + r}{r_s} \right) - \frac{r}{r_s + r} \right]^{-1} \quad (5.14)$$

and r_s is the scale radius of the host halo. Note that in Equation 5.13 the truncation radius, r_t , depends on the 3-dimensional distance to the group centre, r_{sat} , which is not an observable. We draw 3-dimensional radii randomly from an NFW profile given the distribution of projected separations, R_{sat} , for each bin. We additionally force $r_t \leq r_{200}$, although the opposite rarely happens.

We model the truncation itself in a simple fashion, with an NFW profile instantaneously and completely stripped beyond r_t ,

$$\rho_t(r) = \begin{cases} \rho_{\text{NFW}}(r) & r \leq r_t \\ 0 & r > r_t. \end{cases} \quad (5.15)$$

Note that, in addition to r_t , this profile is defined *mathematically* by the same parameters, c and M_{200} , as a regular NFW, even though they are not well-defined physically; when referring to truncated models we report the proper physical masses,

$M_{\text{sub}} \equiv M_{\text{sub}}(< r_t)$. We use the analytical expression for the ESD of the density profile given by Equation 5.15 derived by Baltz et al. (2009). In the leftmost panel of Figure 5.4 we show the ESD corresponding to such profile, compared with the ESD obtained assuming our fiducial NFW profile. The sharp truncation of the profile creates a glitch in the ESD around satellite galaxies at the radius of truncation which is continuous but non-differentiable and which, given our errorbars (cf. Figure 5.1), has no impact on our results. The other panels show the effect of the three parameters describing the truncated subhalo density profile, Equation 5.15 (the full NFW profile follows the same description but without the sharp cut at r_t): as for the group profile, the mass and concentration affect the normalization and slope of the profile, respectively; the rightmost panel shows changes in r_t for the same subhalo mass *within* r_t , which is why the normalization of the different curves is different.

5.4 Results

We show the ESD around satellites in each of the three radial bins in Figure 5.5. Qualitatively, the signal looks similar to that of Figure 5.1, and the features described in Section 5.3 are clearly seen in each of the panels. The dip in the signal close to the typical R_{sat} is smooth, as anticipated in Section 5.3.2, and moves to higher R with increasing R_{sat} , as expected. As in Figure 5.1, the errorbars correspond to the square root of the diagonal elements of the covariance matrix (see Section 5.A).

After describing the fitting procedure in Section 5.4.1, we summarize our constraints on group properties in Section 5.4.2 and on the satellite masses in Section 5.4.3. In Section 5.4.4 we carry out a proof-of-concept comparison of our results to predictions from semi-analytical models of subhalo statistics and we discuss the effect of contamination in the group sample in Section 5.4.5.

5.4.1 Fitting procedure

We fit the data in Figure 5.5 with the model described in Section 5.3 for each of the radial bins, using the median redshift of each galaxy sample, $\langle z_{\text{sat}} \rangle$, as listed in Table 5.1. We use a single normalization f_c^{host} for the $c(M, z)$ relation of groups in the three bins. Our model therefore has seven free parameters: the three (weighted average) masses of the satellites, the three group masses, and a normalization to the $c(M, z)$ relation of Duffy et al. (2008) which applies to all groups across satellite radial bins.

We implement the model described above in a Markov Chain Monte Carlo

(MCMC) using `emcee`⁷ (Foreman-Mackey et al. 2013), which is based on an affine-invariant ensemble sampler. This sampler works by using a number of ‘walkers’ (in our case, a few hundred), each of which starts at a slightly different position in parameter space. Each step is drawn for each walker from a Metropolis-Hastings proposal based on the positions of all other walkers at the previous step (see Goodman & Weare 2010, for details about the algorithm). The likelihood \mathcal{L} is given by

$$\mathcal{L} = \frac{1}{(2\pi)^{9/2}} \prod_{m=1}^3 \prod_{n=1}^3 \frac{1}{\sqrt{|C_{mn}|}} \exp \left[-\frac{1}{2} (\mathbf{O} - \mathbf{E})_m^T C_{mn}^{-1} (\mathbf{O} - \mathbf{E})_n \right], \quad (5.16)$$

where \mathbf{O}_m and \mathbf{E}_m are the measurements and model predictions in radial bin m , respectively; C_{mn}^{-1} is the element of the inverse covariance matrix that accounts for the correlation between radial bins m and n ; and $|C_{mn}|$ is the corresponding determinant. We therefore account for covariance both within and between radial bins in our MCMC. We assume flat, broad priors for all parameters, as listed in Table 5.2.

The data are well fit by the model of Section 5.3. The best-fit model is shown in Figure 5.5 and gives $\chi^2 = 24.7$ with 28 degrees of freedom, with a probability to exceed PTE = 0.64. Joint 2-dimensional posterior distributions for the seven free parameters are shown⁸. Marginalized posterior estimates for all seven parameters, together with 68% credible intervals, are reported in Table 5.2, which also lists the stellar mass fractions, fractional satellite masses, and group mass-to-light ratios derived from the posterior mass estimates.

5.4.2 Group masses and mass-concentration relation

Before discussing the results for the satellite galaxies, we explore the constraints on group masses and the group $c(M, z)$ relation. The masses of the same galaxy groups have been directly measured by Viola et al. (2015), which provides a valuable sanity check of our estimates.

We find that the normalization of the $c(M, z)$ relation is significantly lower than the fiducial Duffy et al. (2008) relation, $f_c^{\text{host}} = 0.53_{-0.14}^{+0.19}$ (where the fiducial value is $f_c^{\text{host}} = 1$). This normalization implies concentrations $c \approx 3$ for these groups. For comparison, using the same parameterization as we do, Viola et al. (2015) measured $f_c^{\text{host}} = 0.84_{-0.23}^{+0.42}$. Our smaller errorbars are due to the fact that

⁷<http://dan.iel.fm/emcee/current/>

⁸We show and list the results in logarithmic space for convenience, but the analysis has been carried out in linear space and the reported uncertainties correspond to the uncertainties in linear space expressed on a logarithmic scale.

we do not account for several nuisance parameters considered by Viola et al. (2015) in their halo model implementation. Most notably, accounting for miscentring significantly increases the uncertainty on the concentration, since both affect $\Delta\Sigma$ at similar scales (Viola et al. 2015). Indeed, when they do not account for miscentring, Viola et al. (2015) measure $f_c^{\text{host}} = 0.59^{+0.13}_{-0.11}$, consistent with our measurement both in the central value and the size of the errorbars. While this means that our estimate of f_c^{host} is biased, accounting for extra nuisance parameters such as miscentring is beyond the scope of this work; our aim is to constrain satellite masses and not galaxy group properties. As shown in Figure 5.6, f_c^{host} is not correlated with any of the other model parameters and therefore this bias in f_c^{host} does not affect our estimates of the satellite masses.

Group masses are consistent with the results from Viola et al. (2015) (with the same caveat that the small errorbars are an artifact produced by our simplistic modelling of the host groups). Specifically, our average mass-to-light ratios follow the mass-luminosity relation found by Viola et al. (2015), $M_{200} \propto L_{200}^{1.16 \pm 0.13}$. As shown in Figure 5.6, group masses are slightly correlated because they are forced to follow the same mass-concentration relation determined by Equation 5.10. Groups in the third bin are on average $\sim 3.4 \pm 0.8$ times more massive than groups in the first radial bin. This is a selection effect, arising because groups in each bin must be big enough to host a significant number of satellites at the characteristic radius of each bin. For example, groups in the first radial bin have⁹ in Figure 5.6 $\log\langle M_{\text{host},1}/(h^{-1}\text{M}_{\odot}) \rangle = 13.46^{+0.06}_{-0.06}$ and $\langle c_1 \rangle \approx 3.3$, which implies a scale radius $\langle r_{s,1} \rangle = 0.19 h^{-1}\text{Mpc}$, beyond which the density drops as $\rho \propto r^{-3}$ (cf. Equation 5.8). The average 3-dimensional distance of satellites to the group centre (see Section 5.3.3) in the third radial bin is $\langle r_{\text{sat},3} \rangle = 0.46 h^{-1}\text{Mpc}$. At this radius, the average density in groups in the first radial bin is seven times smaller than at $\langle r_{s,1} \rangle$.

As mentioned above, our simplistic modelling of groups does not affect the posterior satellite masses significantly. Therefore it is sufficient that our group masses are consistent with the results of Viola et al. (2015), and we do not explore more complex models for the group signal. For a more thorough modelling of the lensing signal of groups in the KiDS-GAMA overlap region, see Viola et al. (2015).

5.4.3 The masses of satellite galaxies

We detect the signal from satellites with significances $>99\%$ in all three radial bins. Satellite masses are consistent across radial bins. We show the marginalized posterior estimates and 68% credible intervals in Figure 5.7 as a function of 3-dimensional group-centric distance, r_{sat} (in units of the group radius r_{200}).

⁹Throughout, we quote masses and radii for a given radial bin by adding an index from 1 to 3 to the subscript of each value.

Table 5.2: Priors, marginalized posterior estimates and derived parameters of the satellites and host groups in the three radial bins. All priors are uniform in linear space in the quoted range. We use medians as central values and all uncertainties are 68% credible intervals. The normalization of the group $c(M, z)$ relation, f_c^{host} , is the same for the three radial bins. The best-fit model has $\chi^2 = 24.7$ with 28 degrees of freedom (PTE = 0.64).

Parameter	Units	Prior	Bin 1	Bin 2	Bin 3
$\log M_{\text{sub}}$	$h^{-1} \text{M}_{\odot}$	[7, 13]	$11.84^{+0.24}_{-0.34}$	$11.84^{+0.24}_{-0.35}$	$12.18^{+0.19}_{-0.24}$
f_c^{host}	1	[0, 2]	$0.53^{+0.19}_{-0.14}$	✓	✓
$\log M_{\text{host}}$	$h^{-1} \text{M}_{\odot}$	[10, 15]	$13.58^{+0.07}_{-0.07}$	$13.62^{+0.07}_{-0.08}$	$14.11^{+0.07}_{-0.07}$
Derived Parameters					
$\langle M_{\star, \text{sat}} \rangle / \langle M_{\text{sub}} \rangle$	h^{-1}	—	$0.04^{+0.02}_{-0.03}$	$0.04^{+0.02}_{-0.03}$	$0.03^{+0.01}_{-0.02}$
$\langle M_{\text{sub}} / M_{\text{host}} \rangle$	1	—	$0.018^{+0.014}_{-0.010}$	$0.016^{+0.013}_{-0.009}$	$0.012^{+0.007}_{-0.005}$
$\langle M_{\text{host}} \rangle / \langle L_{\text{host}} \rangle$	$h \text{M}_{\odot} / \text{L}_{\odot}$	—	300^{+49}_{-45}	265^{+46}_{-42}	386^{+66}_{-61}

Figure 5.7 also shows the subhalo mass as a function of 3-dimensional separation from the group centre found in numerical simulations by Gao et al. (2004). Note that we compare here only the trend with radius, not the normalization. Fitting a power law, $M_{\text{sub}} \propto (r_{\text{sat}}/r_{200})^a$, to the data in Figure 5.7 we find $a = 0.3 \pm 0.5$ (ignoring horizontal errorbars), consistent with the trend predicted by Gao et al. (2004) but also with no dependence on group-centric distance. The bottom panel shows the average stellar mass fractions, which are also consistent with each other, $\langle M_{\star, \text{sat}} / M_{\text{sub}} \rangle \sim 0.04 h^{-1}$.

We also show in Figure 5.7 the results obtained for the truncated theoretical model. The difference between each pair of points depends on the posterior r_t estimated in each bin through Equation 5.13. Specifically, we find $\langle r_t \rangle = \{0.04^{+0.02}_{-0.01}, 0.06^{+0.03}_{-0.02}, 0.09^{+0.04}_{-0.02}\} h^{-1} \text{Mpc}$. We remind the reader that these are theoretical predictions from Equation 5.13 rather than observational results. For comparison, we also show in Figure 5.7 the masses obtained by integrating the posterior NFW models up to said truncation radii, shown by the dashed line. These masses are fully consistent with the truncated model, implying that the difference between the black and grey points (which show $M_{\text{sub}}(< r_{200})$ and $M_{\text{sub}}(< r_t)$, respectively) in Figure 5.7 is only a matter of presentation; the data cannot distinguish between these two models.

After we submitted this work, Li et al. (2016) presented similar, independent satellite lensing measurements. They used $\sim 7,000$ satellites in the redMaPPer galaxy group catalogue (Rykoff et al. 2014) with background sources from CS82 and also measured the lensing signal in three bins in projected radius. They find comparable constraints that are consistent with ours.

5.4.4 The average subhalo mass

We can link the results presented in [Section 5.4.3](#) to predictions from numerical simulations. Comparisons of the satellite populations of observed galaxies (or groups) provide valuable insights as to the relevant physical processes that dominate galaxy formation, as highlighted by the well known ‘missing satellites’ ([Klypin et al. 1999](#); [Moore et al. 1999](#)) and ‘too big to fail’ ([Boylan-Kolchin et al. 2011](#)) problems, which suggest either that our Universe is not well described by a Λ CDM cosmology, or that using numerical simulations to predict observations is more complicated than anticipated. While the former may in fact be true, the latter is now well established, as the formation of galaxies inside dark matter haloes depends strongly on baryonic physics not included in N -body simulations, and the influence of baryons tends to alleviate these problems ([Zolotov et al. 2012](#)).

Here we specifically compare the average subhalo-to-host mass ratio, $\psi \equiv M_{\text{sub}}/M_{\text{host}}$, to Λ CDM predictions through the subhalo mass function, which describes the mass distributions of subhaloes for a given dark matter halo mass. In numerical simulations, the resulting subhalo mass function is a function only of ψ (e.g., [van den Bosch et al. 2005](#); [Jiang & van den Bosch 2016](#)). As summarized in [Table 5.2](#), we find typical subhalo-to-host mass ratios in the range $\langle\psi\rangle \sim 0.015$, statistically consistent across group-centric distance. We obtain these values by taking the ratio $M_{\text{sub}}/M_{\text{host}}$ at every evaluation in the MCMC. For comparison, the values we obtain using the truncated model are $\langle\psi_{\text{tNFW}}\rangle \approx 0.005$, also consistent across radial bins.

We compare our results to the analytical *evolved* (that is, measured after the subhaloes have become satellites of the host halo, as opposed to one measured at the time of infall) subhalo mass function proposed by [van den Bosch et al. \(2005\)](#),

$$\frac{dN}{d\psi} \propto \frac{1}{\psi} (\beta/\psi)^\alpha \exp(-\psi/\beta), \quad (5.17)$$

where $\alpha = 0.9$ and $\beta = 0.13$, and calculate the average subhalo-to-host mass ratio,

$$\langle\psi\rangle = \left[\int_{\psi_{\min}}^{\psi_{\max}} \frac{dN}{d\psi} d\psi \right]^{-1} \int_{\psi_{\min}}^{\psi_{\max}} \psi \frac{dN}{d\psi} d\psi, \quad (5.18)$$

where $\psi_{\min} \approx 10^{-3}$ is approximately the minimum fractional satellite mass we observe given the results of [Section 5.4.3](#), and $\psi_{\max} = 1$ is the maximum fractional satellite mass by definition. Integrating in this range gives $\langle\psi\rangle = 0.0052$.

There are many uncertainties involved in choosing a ψ_{\min} representative of our sample, such as survey incompleteness and the conversion between stellar and total mass; we defer a proper modelling of these uncertainties to future work. For

reference, changing ψ_{\min} by a factor 5 modifies the predicted $\langle\psi\rangle$ by a factor ~ 3 . Considering the uncertainties involved, all we can say at present is that our results are consistent with Λ CDM predictions.

5.4.5 Sensitivity to contamination in the group catalogue

Two sources of contamination in the group catalogue have been neglected in this analysis. The spectroscopic group satellite catalogue used in this work has a high, but not 100%, purity. For groups with $N_{\text{FoF}} \geq 5$ the purity approaches 90%; groups with fewer members have significantly lower purity (Robotham et al. 2011). Li et al. (2013) have shown that a contamination fraction of 10% in the satellite sample would lead to a +15% bias in the inferred satellite masses, well within the reported uncertainties (which amount to up to a factor two).

The second source of contamination is the misidentification of the central galaxy in a group, such that the true central galaxy would be included in our satellite sample. This effect is similar to that explained above, except that contaminating galaxies now reside in particularly massive halos (namely, the groups themselves). Based on comparisons to GAMA mock galaxy catalogues, Robotham et al. (2011) found that the fraction of BCGs correctly identified with the central galaxy of dark matter halos is around 70 – 75% for groups with $N_{\text{FoF}} \geq 5$. Viola et al. (2015) have directly measured the offset probability of BCGs from the true minimum of the potential well. They found that the BCG is as good a proxy for the centre as the iterative centre of Robotham et al. (2011), which according to mock group catalogues are well centred in $\sim 90\%$ of the groups. There are very few groups with $N_{\text{FoF}} \gg 5$ (Robotham et al. 2011), and therefore the lensing signal of a central galaxy in our sample would probably have $\Delta\Sigma(R \approx 0.05 h^{-1}\text{Mpc}) \approx 100 h \text{ M}_{\odot} \text{ pc}^{-2}$ (see Figure 7 of Viola et al. 2015). If we assume (conservatively) that 20% of the BCGs do not correspond to the central galaxy in their groups, then $0.20/7 = 3\%$ (where $\langle N_{\text{FoF}} \rangle \sim 7$, cf. Table 5.1) of our satellites would be central galaxies. Therefore the total signal in the inner regions ($R \approx 0.05 h^{-1}\text{Mpc}$) would be $\Delta\Sigma_{\text{tot}} = 0.03 \times 100 + 0.97 \times \Delta\Sigma_{\text{sub}}^{\text{true}} \simeq 40 h \text{ M}_{\odot} \text{ pc}^{-2}$, which yields $\Delta\Sigma_{\text{sub}}^{\text{true}} = 38 h \text{ M}_{\odot} \text{ pc}^{-2}$. Therefore central galaxy misidentification induces a +5% bias on the signal, which implies roughly a +15% bias on the mass.

Together, these two effects add up to a $\sim 20 - 25\%$ bias in our satellite mass estimates. Such a bias is safely within our statistical uncertainties. Therefore our results are insensitive to plausible levels of contamination in the group catalogue, both from satellites that are not really group members and from misidentified central galaxies.

5.5 Conclusions

We used the first 100 deg² of optical imaging from KiDS to measure the excess surface mass density around spectroscopically confirmed satellite galaxies from the GAMA galaxy group catalogue. We model the signal assuming NFW profiles for both host groups and satellite galaxies, including the contribution from the stellar mass for the latter in the form of a point source. Taking advantage of the combination of statistical power and high image quality, we split the satellite population into three bins in projected separation from the group centre, which serves as a (high-scatter) proxy for the time since infall. We fit the data with a model that includes the satellite and group contributions using an MCMC (see [Section 5.3](#) and [Figure 5.5](#)), fully accounting for the data covariance. As a consistency check, we find group masses in good agreement with the weak lensing study of GAMA galaxy groups by [Viola et al. \(2015\)](#), even though we do not account for effects such as miscentring or the contribution from stars in the BCG.

This model fits the data well, with $\chi^2/\text{d.o.f.} = 0.88$ (PTE = 0.64). We are able to constrain total satellite masses to within ~ 0.3 dex or better. Given these uncertainties, the estimated masses are insensitive to the levels of contamination expected in the group catalogue. Satellite galaxies have similar masses across group-centric distance, consistent with what is found in numerical simulations (accounting for the measured uncertainties). Satellite masses as a function of group-centric distance are influenced by a number of effects. Tidal stripping acts more efficiently closer to the group centre, while dynamical friction makes massive galaxies sink to the centre more efficiently, an effect referred to as mass segregation (e.g., [Frenk et al. 1996](#)). In addition, by binning the sample in (projected) group-centric distance we are introducing a selection effect such that outer bins include generally more massive groups, which will then host more massive satellites on average. Future studies with increased precision may be able to shed light on the interplay between these effects by, for instance, selecting samples residing in the same host groups or in bins of stellar mass.

As a proof of concept, we compare our results to predictions from N -body simulations. These predict that the subhalo mass function is a function only of the fractional subhalo mass, $\psi \equiv M_{\text{sub}}/M_{\text{host}}$. Our binning in satellite group-centric distance produces a selection effect on host groups, such that each bin probes a (slightly) different group population, which allows us to test such prediction. The average fractional mass in all three bins is consistent with a single value (within large errorbars), $\langle\psi\rangle \sim 0.015$. This is broadly consistent with the predictions of numerical simulations. We anticipate that weak lensing of satellite galaxies will become an important tool to constrain the physical processes incorporated in semi-

analytic models of galaxy formation and, ultimately, hydrodynamical simulations.

5.A Full satellite lensing correlation matrix and the contribution from sample variance

As mentioned in [Section 5.3.1](#), we calculate the covariance matrix directly from the data including only the contribution from shape noise (see [Section 3.4](#) of [Viola et al. 2015](#)). In [Figure 5.8](#) we show the corresponding correlation matrix, defined as

$$\mathbf{C}'_{mnij} = \frac{C_{mnij}}{\sqrt{C_{mmii}C_{nnjj}}}, \quad (5.19)$$

where C_{mnij} is the covariance between the i -th and j -th elements of radial bins m and n , respectively (where $m, n = 1, 2, 3$). In reality the lensing covariance also includes a contribution from sample (‘cosmic’) variance, but we have ignored it in our analysis. Below we justify this decision.

The contribution from sample variance can in principle be estimated by bootstrapping the lensing signal over individual KiDS fields. However, there are two caveats to this approach. First, the 101 KiDS fields used here do not produce enough independent bootstrap samples to properly estimate the full covariance matrix for our satellite samples, which is a symmetric 36×36 matrix (containing 648 independent elements) including sample variance for the three radial bins. Second, using single KiDS fields as bootstrap elements means that the elements are not truly independent from each other, because lenses in one field do contribute to signal in neighbouring fields. In fact, we calculate the lensing signal of each galaxy including background galaxies in neighbouring fields.

The latter point is not crucial for our analysis since, as shown in [Figure 5.5](#), the signal produced by satellite subhaloes is confined to the smallest scales, $R \lesssim 0.3 h^{-1}\text{Mpc}$. Therefore, we can estimate the relative contribution from sample variance to the covariance matrix by comparing the diagonal sub-panels of the covariance matrices estimated directly from the data (the ‘analytical’ covariance) and by bootstrapping over KiDS fields. Note that the bootstrap covariance also accounts for shape noise in addition to sample variance. Therefore the ratio between the bootstrap and analytical covariances is a measure of the relative contribution of sample variance to the satellite lensing covariance. It should be noted, however, that the bootstrap covariance can be biased high by as much as 40% ([Norberg et al. 2009](#)).

We show this comparison in [Figure 5.9](#) for each of the three radial bins, where we compare $\sqrt{C_{mmii}}$ estimated from the analytic (i.e., data) and bootstrap covariances. Both methods lead to similar values up to the largest angular separa-

tions. There is a hint of a nonzero contribution from sample variance at scales $R > 0.3 h^{-1}\text{Mpc}$, where the bootstrap variance is $\sim 10\%$ larger than the analytical variance. As stated above, the satellite contribution to $\Delta\Sigma$ is confined to scales smaller than these. We conclude that, for the purpose of this work, we can safely ignore sample variance.

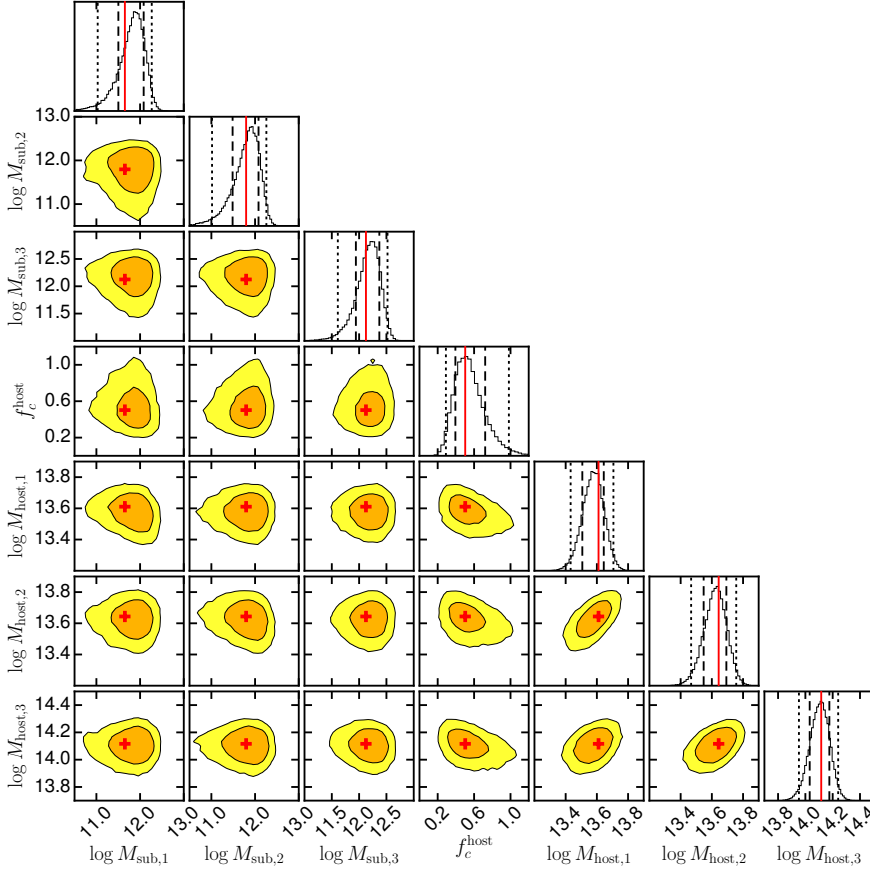


Figure 5.6: Joint 2-dimensional (lower off-diagonal panels, with contours at 68% and 95% joint credible regions) and marginalized 1-dimensional (diagonal panels) posterior distributions of free parameters of the model described in [Section 5.3](#), with subhaloes modelled with NFW density profiles. In the diagonal panels, black dashed and dotted lines mark marginalized 68% and 95% credible intervals, respectively, and vertical red solid lines mark the maximum likelihood estimate. Red crosses in off-diagonal panels show the joint best-fit values. All masses are in units of $h^{-1}M_{\odot}$ and are numbered according to the radial bin to which they correspond.

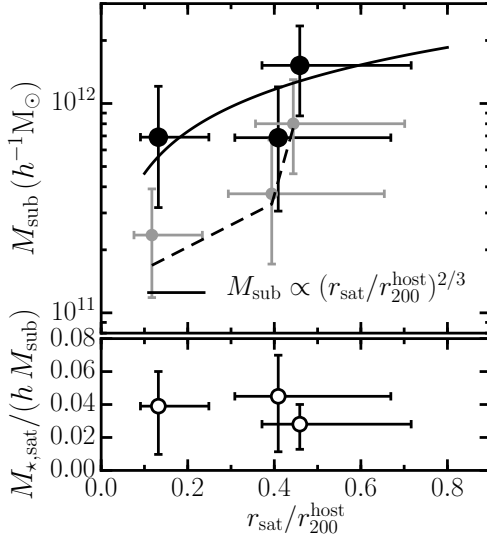


Figure 5.7: Top: Marginalized posterior mass estimates of satellite galaxies from the full NFW (black, large points) and truncated NFW (grey, small points) models, and the dashed black line shows the NFW masses within the same truncation radii for comparison. Horizontal error-bars are 68% ranges in (3-dimensional) r_{sat}/r_{200} per bin. The black solid line shows the radial dependence of subhalo mass predicted by the numerical simulations of Gao et al. (2004) with an arbitrary normalization. Bottom: Stellar-to-total mass ratios in each bin.

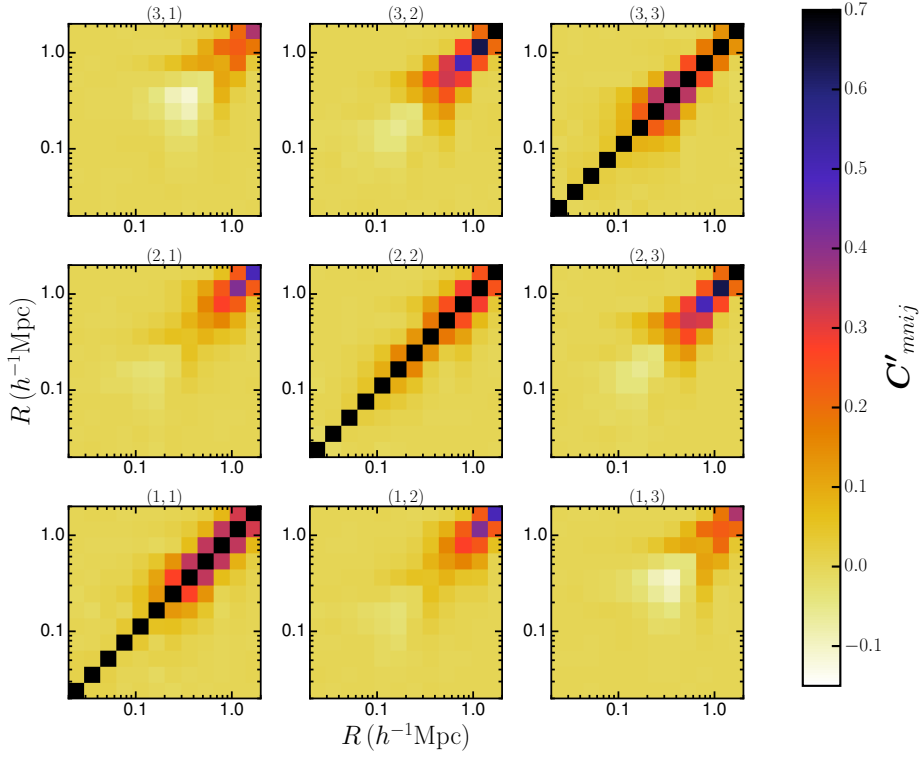


Figure 5.8: Full satellite lensing correlation matrix within and between radial bins as shown by the label at the top of each plot.

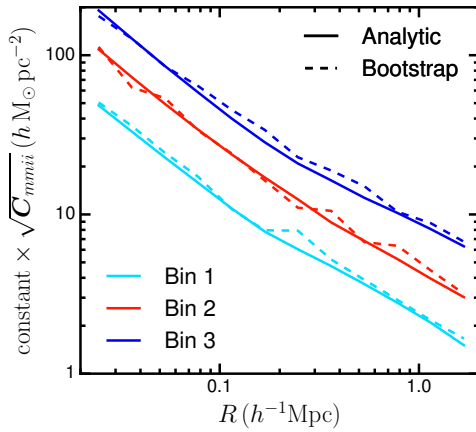


Figure 5.9: Comparison of the variances calculated analytically (solid), which account only for shape noise, and by bootstrapping (dashed), which also account for sample variance, for the diagonal subpanels of the covariance matrix as per [Figure 5.8](#). The red and blue lines have been offset vertically for clarity.

Bibliography

- Abazajian K. N., et al., 2009, *ApJS*, **182**, 543
- Aihara H., et al., 2011, *ApJS*, **193**, 29
- Baldry I. K., et al., 2010, *MNRAS*, **404**, 86
- Balestra I., et al., 2010, *A&A*, **512**, A12
- Baltz E. A., Marshall P., Oguri M., 2009, *JCAP*, **1**, 015
- Benítez N., 2000, *ApJ*, **536**, 571
- Benjamin J., et al., 2013, *MNRAS*, **431**, 1547
- Bertin E., Arnouts S., 1996, *A&AS*, **117**, 393
- Binney J., Tremaine S., 1987, Galactic dynamics
- Boylan-Kolchin M., Bullock J. S., Kaplinghat M., 2011, *MNRAS*, **415**, L40
- Brainerd T. G., Blandford R. D., Smail I., 1996, *ApJ*, **466**, 623
- Bruzual G., Charlot S., 2003, *MNRAS*, **344**, 1000
- Chang J., Macciò A. V., Kang X., 2013a, *MNRAS*, **431**, 3533
- Chang C., et al., 2013b, *MNRAS*, **434**, 2121
- Comparat J., et al., 2013, *MNRAS*, **433**, 1146
- Contini E., De Lucia G., Borgani S., 2012, *MNRAS*, **420**, 2978
- Courteau S., et al., 2014, *Reviews of Modern Physics*, **86**, 47
- Driver S. P., et al., 2011, *MNRAS*, **413**, 971
- Duffy A. R., Schaye J., Kay S. T., Dalla Vecchia C., 2008, *MNRAS*, **390**, L64
- Einasto J., 2013, *Brazilian Journal of Physics*, **43**, 369
- Erben T., et al., 2013, *MNRAS*, **433**, 2545
- Foreman-Mackey D., Hogg D. W., Lang D., Goodman J., 2013, *PASP*, **125**, 306
- Frenk C. S., Evrard A. E., White S. D. M., Summers F. J., 1996, *ApJ*, **472**, 460
- Gao L., White S. D. M., Jenkins A., Stoehr F., Springel V., 2004, *MNRAS*, **355**, 819
- Gillis B. R., et al., 2013, *MNRAS*, **431**, 1439
- Goodman J., Weare J., 2010, *Communications in Applied Mathematics and Computational Science*, **5**, 65
- Hayashi E., Navarro J. F., Taylor J. E., Stadel J., Quinn T., 2003, *ApJ*, **584**, 541
- Heymans C., et al., 2012, *MNRAS*, **427**, 146
- Hildebrandt H., et al., 2012, *MNRAS*, **421**, 2355

- Hoekstra H., Franx M., Kuijken K., 2000, *ApJ*, **532**, 88
- Jiang F., van den Bosch F. C., 2016, *MNRAS*, **458**, 2848
- King I., 1962, *AJ*, **67**, 471
- Kitching T. D., Miller L., Heymans C. E., van Waerbeke L., Heavens A. F., 2008, *MNRAS*, **390**, 149
- Klypin A., Gottlöber S., Kravtsov A. V., Khokhlov A. M., 1999, *ApJ*, **516**, 530
- Kuijken K., 2008, *A&A*, **482**, 1053
- Kuijken K., et al., 2015, *MNRAS*, **454**, 3500
- Li R., Mo H. J., Fan Z., Yang X., Bosch F. C. v. d., 2013, *MNRAS*, **430**, 3359
- Li R., et al., 2014, *MNRAS*, **438**, 2864
- Li R., et al., 2016, *MNRAS*, **458**, 2573
- Libeskind N. I., Di Cintio A., Knebe A., Yepes G., Gottlöber S., Steinmetz M., Hoffman Y., Martinez-Vaquero L. A., 2013, *PASA*, **30**, e039
- Lilly S. J., et al., 2007, *ApJS*, **172**, 70
- Limousin M., Kneib J. P., Bardeau S., Natarajan P., Czoske O., Smail I., Ebeling H., Smith G. P., 2007, *A&A*, **461**, 881
- Liske J., et al., 2015, *MNRAS*, **452**, 2087
- Mamon G. A., Biviano A., Murante G., 2010, *A&A*, **520**, A30
- McFarland J. P., Verdoes-Kleijn G., Sikkema G., Helmich E. M., Boxhoorn D. R., Valentijn E. A., 2013, *Experimental Astronomy*, **35**, 45
- Melchior P., Viola M., 2012, *MNRAS*, **424**, 2757
- Miller L., Kitching T. D., Heymans C., Heavens A. F., van Waerbeke L., 2007, *MNRAS*, **382**, 315
- Miller L., et al., 2013, *MNRAS*, **429**, 2858
- Mo H., van den Bosch F. C., White S., 2010, *Galaxy Formation and Evolution*
- Moore B., Ghigna S., Governato F., Lake G., Quinn T., Stadel J., Tozzi P., 1999, *ApJL*, **524**, L19
- Natarajan P., Kneib J.-P., Smail I., 2002, *ApJL*, **580**, L11
- Natarajan P., De Lucia G., Springel V., 2007, *MNRAS*, **376**, 180
- Natarajan P., Kneib J.-P., Smail I., Treu T., Ellis R., Moran S., Limousin M., Czoske O., 2009, *ApJ*, **693**, 970
- Navarro J. F., Frenk C. S., White S. D. M., 1995, *MNRAS*, **275**, 720
- Norberg P., Baugh C. M., Gaztañaga E., Croton D. J., 2009, *MNRAS*, **396**, 19
- Pastor Mira E., Hilbert S., Hartlap J., Schneider P., 2011, *A&A*, **531**, A169
- Planck Collaboration 2015, preprint, ([arXiv:1502.01589](https://arxiv.org/abs/1502.01589))
- Refregier A., Kacprzak T., Amara A., Bridle S., Rowe B., 2012, *MNRAS*, **425**, 1951
- Robotham A. S. G., et al., 2011, *MNRAS*, **416**, 2640
- Romano-Díaz E., Shlosman I., Heller C., Hoffman Y., 2010, *ApJ*, **716**, 1095
- Rozo E., Rykoff E. S., Becker M., Reddick R. M., Wechsler R. H., 2015, *MNRAS*, **453**, 38
- Rykoff E. S., et al., 2014, *ApJ*, **785**, 104
- Schewtschenko J. A., Macciò A. V., 2011, *MNRAS*, **413**, 878

- Schneider P., 2003, *A&A*, 408, 829
- Springel V., et al., 2005, *Nature*, 435, 629
- Taffoni G., Mayer L., Colpi M., Governato F., 2003, *MNRAS*, 341, 434
- Taylor E. N., et al., 2011, *MNRAS*, 418, 1587
- Tormen G., Diaferio A., Syer D., 1998, *MNRAS*, 299, 728
- Trimble V., 1987, *ARA&A*, 25, 425
- Vanzella E., et al., 2008, *A&A*, 478, 83
- Viola M., Kitching T. D., Joachimi B., 2014, *MNRAS*, 439, 1909
- Viola M., et al., 2015, *MNRAS*, 452, 3529
- White S. D. M., Rees M. J., 1978, *MNRAS*, 183, 341
- Wright C. O., Brainerd T. G., 2000, *ApJ*, 534, 34
- Yang X., Mo H. J., van den Bosch F. C., Jing Y. P., Weinmann S. M., Meneghetti M., 2006, *MNRAS*, 373, 1159
- Yang X., Mo H. J., van den Bosch F. C., Pasquali A., Li C., Barden M., 2007, *ApJ*, 671, 153
- York D. G., et al., 2000, *AJ*, 120, 1579
- Zolotov A., et al., 2012, *ApJ*, 761, 71
- de Jong J. T. A., et al., 2013, *The Messenger*, 154, 44
- de Jong J. T. A., et al., 2015, *A&A*, 582, A62
- van Uitert E., et al., 2016, *MNRAS*,
- van den Bosch F. C., Tormen G., Giocoli C., 2005, *MNRAS*, 359, 1029